Geochemistry Geophysics Geosystems G3

Article
Volume 13, Number 1
9 October 2012
Q0AG11, doi:10.1029/2012GC004210
ISSN: 1525-2027

Published by AGU and the Geochemical Society

Seismicity of the Atlantis Massif detachment fault, 30°N at the Mid-Atlantic Ridge

John A. Collins, Deborah K. Smith, and Jeffrey J. McGuire

Department of Geology and Geophysics, Woods Hole Oceanographic Institution, Woods Hole, Massachusetts 02543, USA (jcollins@whoi.edu)

[1] At the oceanic core complex that forms the Atlantis Massif at 30°N on the Mid-Atlantic Ridge, slip along the detachment fault for the last 1.5–2 Ma has brought lower crust and mantle rocks to the seafloor. Hydroacoustic data collected between 1999 and 2003 suggest that seismicity occurred near the top of the Massif, mostly on the southeastern section, while detected seismicity along the adjacent ridge axis was sparse. In 2005, five short-period ocean bottom seismographs (OBS) were deployed on and around the Massif as a pilot experiment to help constrain the distribution of seismicity in this region. Analysis of six months of OBS data indicates that, in contrast to the results of the earlier hydroacoustic study, the vast majority of the seismicity is located within the axial valley. During the OBS deployment, and within the array, seismicity was primarily composed of a relatively constant background rate and two large aftershock sequences that included 5 teleseismic events with magnitudes between 4.0 and 4.5. The aftershock sequences were located on the western side of the axial valley adjacent to the Atlantis Massif and close to the ridge-transform intersection. They follow Omori's law, and constitute more than half of the detected earthquakes. The OBS data also indicate a low but persistent level of seismicity associated with active faulting within the Atlantis Massif in the same region as the hydroacoustically detected seismicity. Within the Massif, the data indicate a north-south striking normal fault, and a left-lateral, strike-slip fault near a prominent, transform-parallel, north-facing scarp. Both features could be explained by changes in the stress field at the inside corner associated with weak coupling on the Atlantis transform. Alternatively, the normal faulting within the Massif might indicate deformation of the detachment surface as it rolls over to near horizontal from an initial dip of about 60° beneath the axis, and the strike-slip events may indicate transform-parallel movement on adjacent detachment surfaces.

Components: 7600 words, 11 figures, 1 table.

Keywords: Atlantis Massif; Mid-Atlantic Ridge; T-phase; hydroacoustic; oceanic detachment fault; seismicity.

Index Terms: 3035 Marine Geology and Geophysics: Midocean ridge processes; 7245 Seismology: Mid-ocean ridges; 7250 Seismology: Transform faults.

Received 24 April 2012; **Revised** 4 September 2012; **Accepted** 5 September 2012; **Published** 9 October 2012.

Collins, J. A., D. K. Smith, and J. J. McGuire (2012), Seismicity of the Atlantis Massif detachment fault, 30°N at the Mid-Atlantic Ridge, *Geochem. Geophys. Geosyst.*, *13*, Q0AG11, doi:10.1029/2012GC004210.

Theme: Oceanic Detachment Faults

1. Introduction

[2] Over the last several years it has been recognized that there are two styles of magmatic seafloor spreading at slow-spreading ocean ridges. Classic magmatic spreading is characterized by magmatic diking, short-offset high-angle faulting, and the formation of linear, ridge-parallel abyssal hills on both ridge flanks. The second style of spreading differs from this in that long-lived faults (detachment faults) unroof lower ocean crust and mantle on one flank of the axis, while the volcanic section is spread away in the opposite direction [*Blackman et al.*, 1998; *Cann et al.*, 1997; *Cannat et al.*, 2006; *Dick et al.*, 1981; *Escartín and Cannat*, 1999; *Ildefonse et al.*, 2007; *Karson*, 1999; *Kelemen et al.*, 2004; *MacLeod et al.*, 2002; *Searle et al.*, 2003; *Tucholke et al.*, 1998]. Where detachment faults are identified at the axis, they are associated with high rates of hydroacoustically recorded seismicity, and are inferred to be actively slipping [*Escartín et al.*, 2008; *Smith et al.*, 2006]. We now understand that detachment faults, which involve significant fault rotation and the formation of core complexes, may account for close to 50% of the extension at the northern MAR between 12°N and 35°N [*Escartín et al.*, 2008].

[3] The Atlantis Massif is an oceanic core complex located at the intersection of the Mid-Atlantic Ridge (MAR) spreading axis and the Atlantis transform fault at 30°N (Figure 1) [*Cann et al.*, 1997]. Slip along the detachment fault for the last 1.5–2 Ma has brought lower crust and mantle rocks to the seafloor [e.g., *Blackman et al.*, 2002, 2011; *Cann et al.*, 1997], and has led to one of the most striking topographic features on the northern MAR, with distinctive spreading-parallel striations marking the overturned and slightly domed exhumed fault surface (Figures 1 and 2). Since the Atlantis Massif was first identified as an oceanic core complex, it has been the subject of many geologic and geophysical studies, and has been drilled during Expeditions 304 and 305 of the Integrated Ocean Drilling Project (IODP) [e.g., *Blackman and Collins*, 2010; *Blackman et al.*, 2002, 2011; *Canales et al.*, 2004, 2008; *Cann et al.*, 1997; *Collins et al.*, 2009; *Grimes et al.*, 2008; *Henig et al.*, 2012; *Ildefonse et al.*, 2007; *Karson et al.*, 2006; *Kelley et al.*, 2001, 2005; *Schroeder and John*, 2004].

[4] Earthquake-generated hydroacoustic signals, T-phases, recorded between 1999 and 2003 [*Smith et al.*, 2002, 2003] suggest that the southeastern section of the Atlantis Massif is seismically active, while activity is limited at the adjacent ridge axis (Figure 1). T-phases propagate efficiently for hundreds of kilometers within the acoustic waveguide that constitutes the SOFAR channel, and are recorded by hydrophones moored within the channel. Because of the uncertainty in models for T-phase excitation and propagation, however, it has been questioned whether the locations determined from the hydrophone-recorded data coincide with earthquake epicenters [e.g., *Williams et al.*, 2006]. *Williams et al.* [2006] suggested three possible explanations for the observed pattern at the Atlantis Massif. 1) Radiated seismic energy from events located beneath the ridge axis propagates through the crust of the Massif and couples preferentially into the water column at the Massif summit, whose shallow top intercepts the SOFAR channel located 850–1000 m below the seafloor. 2) The same number of events occur at all water depths, but a larger number of events are recorded from the summit and the shallow flanks of the Massif because the energy couples more easily into the SOFAR channel there, as above. 3) A greater number of seismic events occur at shallow water depths compared with deeper water depths and are associated with the development and evolution of the Massif. *Williams et al.* [2006] could not discriminate between the three possibilities.

[5] To identify and characterize active deformation associated with the Atlantis Massif detachment fault, and to assess whether the hydroacoustically detected earthquakes might have been located within the Atlantis Massif, we deployed an array of five short-period OBS as a pilot experiment on and around the Massif from June 2005 to March 2006. The OBS reliably record earthquakes with magnitudes as small as 0–0.5, and thus present a more complete view of the seismicity patterns within the region. In this paper we present the earthquake catalogs determined from this data set, as well as composite focal mechanisms for events occurring within the Massif.

2. Geology of the Atlantis Massif

[6] The Atlantis Massif ocean core complex is made up of South Ridge, Central Dome, and a volcanic block east of Central Dome (Figure 1a). South Ridge borders the Atlantis transform, and extends to the edge of the axial valley (Figure 1b). The scarp facing the transform is ~3 km in relief and is deeply eroded. Lost City hydrothermal vent field [e.g., *Kelley et al.*, 2001, 2005] sits on a ledge protruding from the upper part of the south-facing scarp (Figure 1a). On its

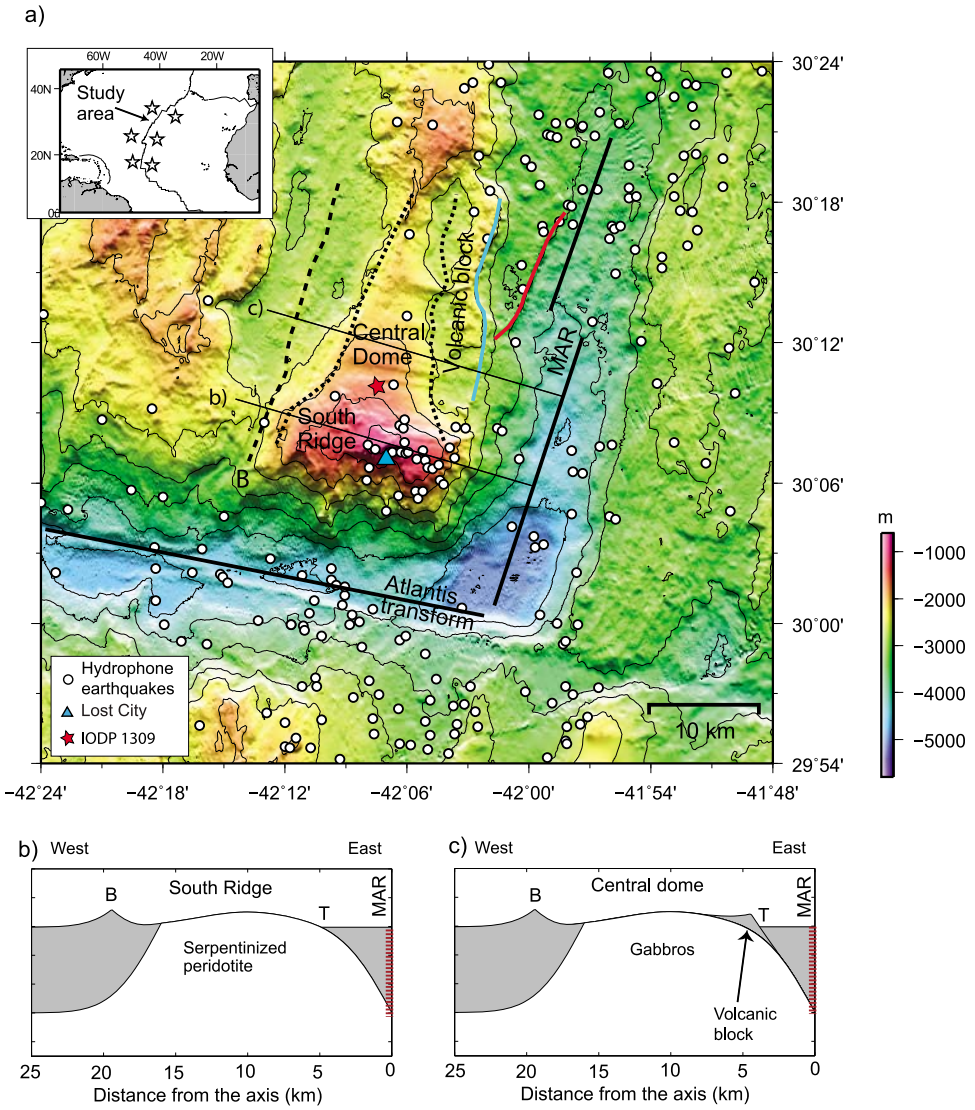

Figure 1. (a) The Atlantis Massif at the intersection of the Atlantis transform and the Mid Atlantic Ridge (MAR) at 30°N. Inset: location map with stars showing the location of 6 autonomous hydrophones that were deployed between 15°N and 35°N from 1999 to 2003 [*Smith et al.*, 2002]. The axes of the transform and rift valley are marked by black lines. White circles: 257 earthquake epicenters determined by the autonomous hydrophone array [*Smith et al.*, 2003]. Blue triangle: Lost City vent field [*Kelley et al.*, 2001, 2005]. B: breakaway (initiation) of detachment fault shown as dashed line. Dotted line: outline of corrugated surface. Blue and red lines: faults defining possible rafted blocks [*Reston and Ranero*, 2011]. Cartoons showing possible cross sections through (b) South Ridge and (c) Central Dome modified from *Smith et al.* [2008]. At Central Dome, a new normal fault at the axis roots into the main detachment, and a section of the median valley floor has been transferred from the hanging wall to the footwall. Gray: crust predating the onset of faulting; white: material drawn up from below by slip on the fault and by fault rotation.

north side, South Ridge is bordered by a transform-parallel, north-facing scarp. Close to the axis, the north-facing scarp has a relief of about 1500 m, while farther west, where South Ridge borders Central Dome, the scarp is not as dramatic and has a relief of ~400 m. The shallowest water depths in the region (~700 m) are on the top of South Ridge. Spreading-parallel striations typical of the exhumed footwalls of oceanic detachment faults [*Cann et al.*, 1997] have been observed on the top of South Ridge [*Blackman et al.*, 2002], and rock samples indicate that the top is composed mainly of serpentinized peridotites with some gabbroic intrusions [*Karson et al.*, 2006].

[7] The Central Dome section of the Atlantis Massif is adjacent to and north of South Ridge. Central Dome is broadly arched, does not rise as high as South Ridge, and has distinctive spreading-parallel striations on its surface. Drilling into Central

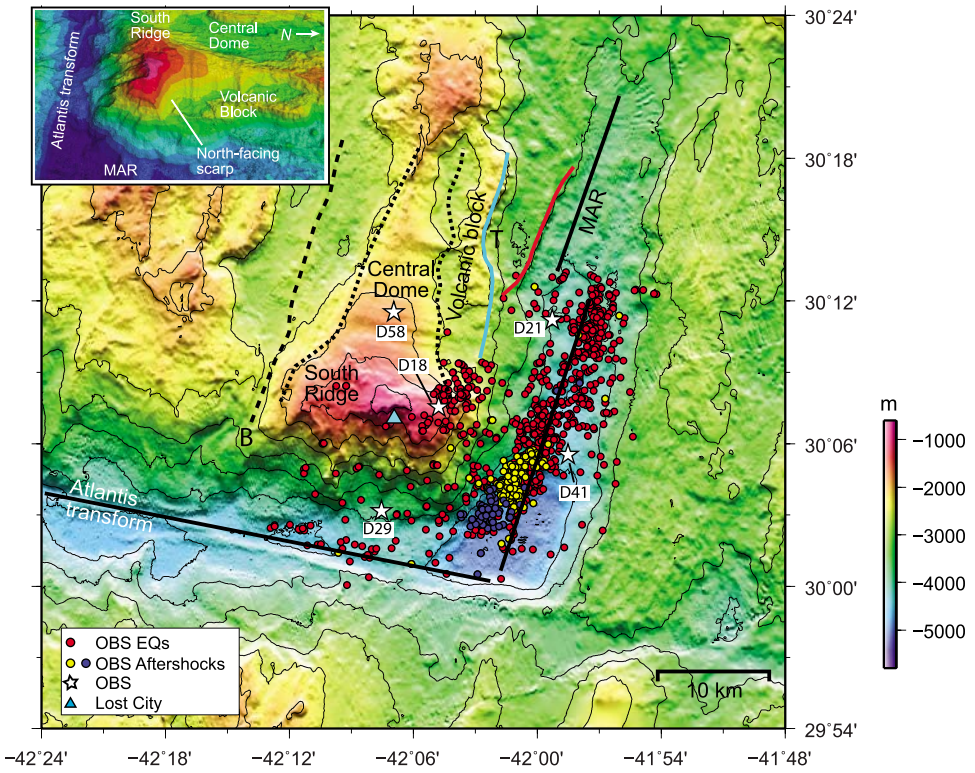

Figure 2. OBS-recorded seismicity at the intersection of the Atlantis transform and the MAR. Interpretation of features as in Figure 1. The red filled circles show epicenters for all well located events occurring during the OBS acquisition period from June through December 2005. The blue and yellow circles show the locations of the July and November 2005 aftershock sequences. OBS-recorded seismicity continues north along the axis but only the ~1100 largest and relocated earthquakes are shown here. White stars: OBS locations, labeled. Blue triangle: Lost City vent field [*Kelley et al.*, 2001, 2005]. Inset: 3-D image of Atlantis Massif from the east, high-lighting the north-facing scarp.

Dome by the IODP [*Expedition Scientific Party*, 2005; *Ildefonse et al.*, 2007] yielded a thick sequence of mainly gabbroic rocks. Central Dome is bordered to the east by a volcanic block. It is possible that a new normal fault has formed at the axis and carried a section of inner valley floor off axis. In this case, the section of the detachment fault that produced Central Dome would no longer be active. Another possibility is that the putative new normal fault roots into the long-lived detachment (Figure 1c) [*Buck*, 1988; *Reston and Ranero*, 2011; *Schouten et al.*, 2010; *Smith et al.*, 2008]. In this case, the block is a triangular section of the median-valley floor hanging wall, referred to as a rafted block, which is transferred from the hanging wall to the footwall of the detachment fault and rafted off axis.

3. Seismic Experiment and Data Analysis

[8] Long-term hydroacoustic monitoring was initiated at the northern MAR in February 1999 [*Smith et al.*, 2002]. Six autonomous hydrophones were moored between 15°N and 35°N on the flanks of the MAR (inset in Figure 1). The array was deployed for over 3 years and recorded T phases – earthquake-generated hydroacoustic waves that can propagate for hundreds of kilometers in the SOFAR channel – from a total of 9,376 earthquakes along the MAR. By comparison, only 7% (626) of these earthquakes were located by land-based seismic networks. *Bohnenstiehl et al.* [2002] concluded that the hydroacoustic data improve the completeness level of the earthquake catalog for the MAR by about 1.5–2.0 orders of magnitude, yielding a magnitude of completeness of about M = 2.5. With the improved detection and the improved location accuracy provided by hydroacoustic techniques (errors of a few kilometers [*Dziak et al.*, 2004; *Pan and Dziewonski*, 2005]), it has been possible to address a number of diverse geologic problems [e.g., *Bohnenstiehl et al.*, 2002; *Dziak et al.*, 2004; *Escartín et al.*, 2008; *Simão et al.*, 2010; *Smith et al.*, 2003; *Williams et al.*, 2006] including the seismic characteristics of inside corner highs and

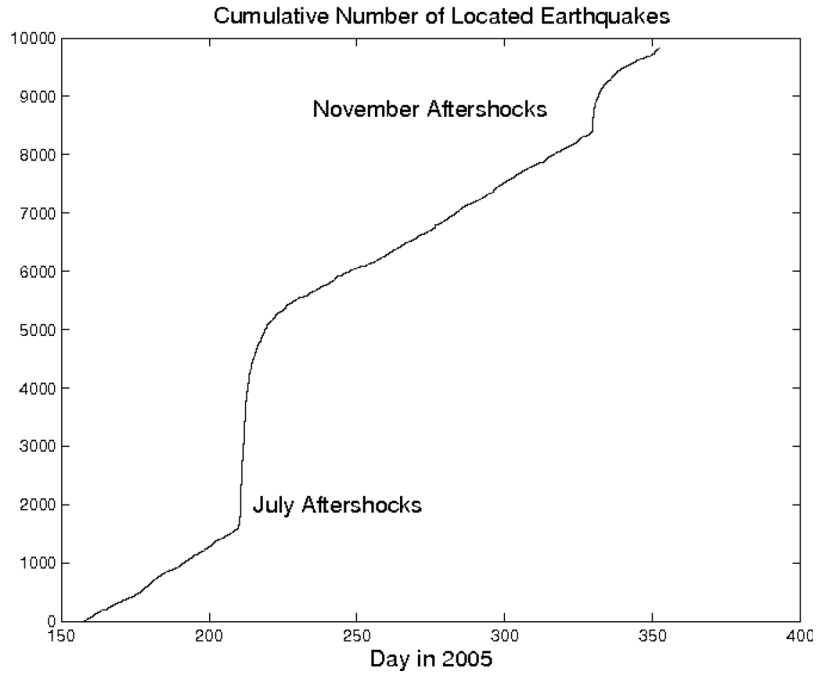

Figure 3. The cumulative number of earthquakes detected and located using automated short-term-average/long-term-average (STA/LTA) detectors and the Antelope software. All earthquakes have at least 7 combined P and S-wave arrival time picks. The July and November aftershock sequences (Figure 2) are superimposed on a relatively constant background seismicity rate.

core complexes such as the Atlantic Massif [*Escartín et al.*, 2008; *Williams et al.*, 2006].

[9] In June 2005, we deployed five short-period OBS in the region of the Atlantis Massif as a pilot seismicity experiment (Figure 2). Each OBS was equipped with a 3-component geophone (4.5 Hz natural frequency) and a hydrophone. Unfortunately, the OBS deployment took place just after the recovery of the large-aperture hydrophone array, so that the two data sets are not concurrent. (A hydrophone array deployed farther north, although overlapping in time with the OBS deployment, did not extend sufficiently far south to allow accurate earthquake locations, and hence was not useful for comparison [*Simão et al.*, 2010].) The OBS array was recovered in March 2006, but the data acquisition period comprised the 6 months from June to December 2005 only. Stations D18, D29, D41, and D58 (Figure 2) all returned high quality data. Estimates of local magnitude indicate that these sites routinely recorded earthquakes down to m_L 0–0.5. The geophone of station D21, however, was poorly coupled to the seafloor, and only the larger ($M > \sim 2$) earthquakes produced clear P- and S-wave signals on the ground-motion sensor. However, the hydrophone for this station performed to specification.

[10] Automated, first-arrival picking and location algorithms were run on the first six months of the data set using the Antelope software package (http://www.brtt.com) and a wavelet-based S-wave arrival picker [*Simons et al.*, 2006]. In the first six months, at least 10,000 locatable earthquakes were recorded. The vast majority of the earthquakes, however, were not clearly observed on station D21 because of its poor coupling. The cumulative number of earthquakes detected and located is shown in Figure 3. All located earthquakes have at least 7 combined P- and S-wave travel time picks. The earthquake associations and initial grid-search locations were done with a standard one-dimensional velocity model for oceanic crust. The first-order feature of the data set is that it is composed of a relatively constant background seismicity rate and two large aftershock sequences (Figures 2 and 3). The aftershock sequences (in July and November 2005) follow clusters of Magnitude 4 earthquakes (Table 1), and are located in the axial valley, adjacent to South Ridge and close to the ridge-transform intersection. They make up more than half of the located earthquakes in the first 6 months of the deployment. Omori's law of aftershock decay is clearly followed by both aftershock sequences (Figure 3). Owing to the very sparse

Table 1. Moderate Earthquakes Recorded by the OBS Array and by the Global Seismic Network (GSN)

Date	Time	Lat	Lon	M_w
06/29/05	04:24:50	30.39	−41.95	4.1
07/07/05	08:20:57	30.06	−42.27	3.9
07/29/05	13:02:44	30.05	−42.02	4.1
07/29/05	13:09:55	30.06	−42.02	4.5
10/28/05	06:05:57	30.14	−42.26	4
11/25/05	11:00:21	30.04	−42.05	4.5
11/25/05	11:40:00	30.03	−42.06	4.4

station spacing, our data set has almost no control on earthquake depth; the arrival times are generally consistent with earthquakes in the lower crust (assuming ordinary Vp/Vs ratios) but we do not interpret the range of depths found by the location algorithm owing to the poor constraint on source depth.

[11] To accurately image the faulting geometry responsible for the abundant microseismicity, we relocated a subset of 1178 earthquakes using waveform-derived differential arrival times, which provided relative travel times with an accuracy of better than 0.02 s (Figure 4). We applied the HYPODD relative location algorithm to this subset of 1178 earthquakes, using the improved travel-time picks [*Waldhauser*, 2001; *Waldhauser and Ellsworth*, 2000]. We only included waveform cross-correlation derived relative arrival-time picks (coefficient cutoff >0.7) [*Schaff et al.*, 2002, 2004], of which there were over 600,000. This method works very well with the data set. The relative locations also minimize errors from un-modeled 3-D velocity structure, which is likely to be significant here based on existing 2-D reflection/refraction experiments [*Blackman and Collins*, 2010; *Canales et al.*, 2007; *Collins et al.*, 2009].

4. Observed Seismicity Distribution

[12] The epicenters of the relocated earthquakes are shown in Figure 2. OBS-recorded seismicity continues north along the axis, but only the ∼1100 largest and relocated earthquakes are shown here. In contrast to the results of the hydroacoustic experiment, the OBS data indicate abundant seismicity within the axial rift valley just north of the transform. This difference suggests either that: (i) seismicity in this segment is episodic, with either the OBS experiment taking place in an unusually active period or the hydroacoustic experiment coinciding with an unusually quiet period; (ii) seismic energy from events in this deep section of the axial valley does not couple well into the water column and hence is not well recorded by the hydroacoustic array; or (iii) seismic energy from events in this deep section of the axial valley couple preferentially into the water column at locations on the Massif where the seafloor projects into the axis of the SOFAR channel.

[13] An assessment of the relative magnitudes of the OBS recorded earthquakes indicates that all of the large earthquakes (ml > 2.5) occurred within the axial valley or along the transform fault. There are no ml > 2.5 earthquakes located within the cluster of events on the top of the Massif during our deployment. In addition, inspection of Figure 1 shows that the hydroacoustic array detected and located abundant seismicity from the shallower section of the axial valley immediately north of the OBS deployment indicating that the hydrophone array does

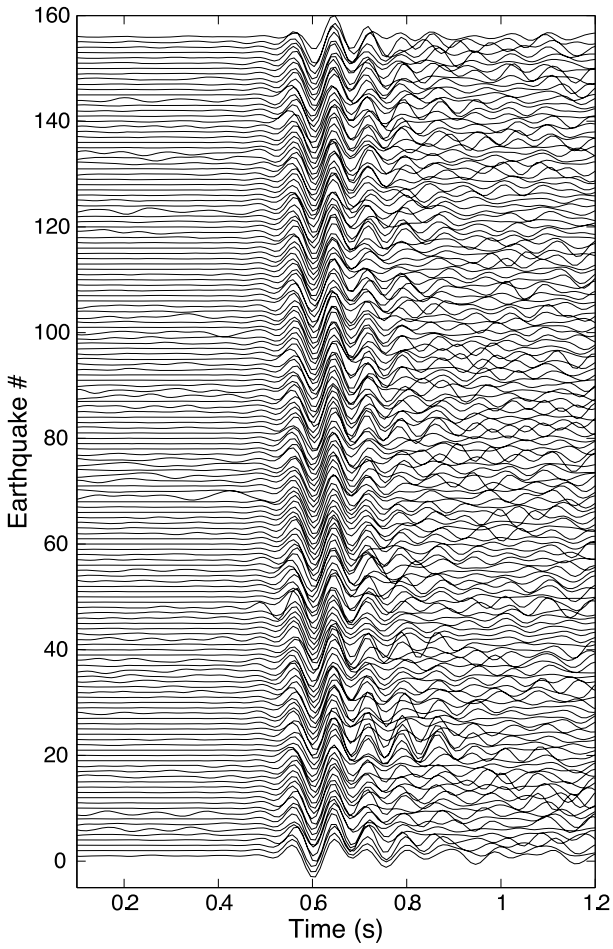

Figure 4. Examples of differential arrival times derived from waveform cross-correlation. P waveforms from station D18 for a family of about 160 aftershocks of the July 28th Mw 4.5 earthquake with similar P waves (cc > 0.8) aligned by cross-correlation. We are able to measure relative arrival times to ∼0.02 s.

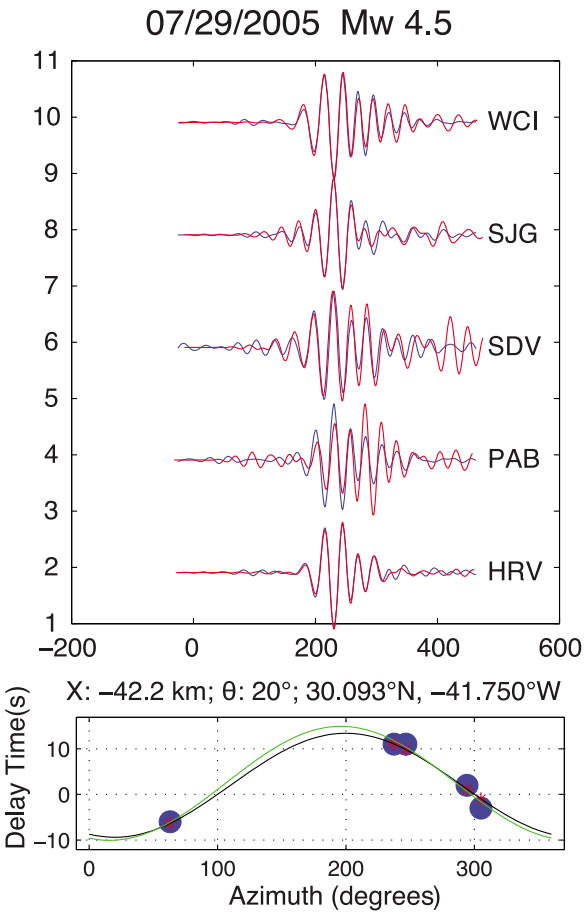

Figure 5. (top) Example of Rayleigh-waveform cross-correlations between the main shock of the July 2005 sequence (red traces) and those from an Mw 5 event in 1995 (blue traces) that has a seismic moment estimate from the global CMT catalog. (bottom) The variation in relative arrival times results from the spatial separation in event centroid locations. The traces have been scaled to the same amplitude for plotting purposes. The absolute amplitudes of their cross-correlation are used to estimate the seismic moment of the 2005 event. Similar analysis was done for the other events in Table 1.

record axial valley earthquakes. Taken together the above observations suggest that the energy from earthquakes occurring within the deeper sections of the ridge axis is not reaching the SOFAR channel and not being recorded by the hydrophones. The difference in epicentral distributions between Figures 1 and 2 likely results from a combination of undetected events (in the T-phase catalog) in the deeper portion of the axial valley and possibly events whose T-phase radiator position is significantly offset from their epicenter due to the extreme range of seafloor topography in this region.

[14] Several of the earthquakes recorded by the OBS array were large enough to have clear Rayleigh wave recordings on numerous Global Seismic Network (GSN) stations (Figure 5). We estimated their moment magnitudes using a Rayleigh-wave Empirical Green's Function (EGF) technique [*McGuire*, 2008]. In this approach, waveforms from a nearby large earthquake that is in the Global CMT catalog are cross-correlated with the data from the smaller event of interest to determine its relative location and magnitude (Figure 5). The location and magnitude estimates from this approach for the seven largest earthquakes in our data set are given in Table 1. The high degree of waveform similarity between these events and a M5.5 normal fault event in the Global CMT catalog (Figure 5) confirm that the largest events in our data set, all of which are located within the median valley, occurred on normal faults.

[15] The OBS data also address the extent to which there is ongoing deformation within the Atlantis Massif. The relocated seismicity shows earthquakes along much of South Ridge throughout the 6-month data acquisition period (Figure 2). These events have easily picked P- and S-wave arrivals at station D18 with short S-P times (<=1.0 s) that conclusively demonstrate that there is active faulting within the Massif (Figure 6). The nature of this faulting is addressed in the next section. The asymmetry in seismicity seen in Figure 2, from the inside-corner to the west, across the axial valley, and onto the outside corner to the east, is similar to the across-axis asymmetry associated with the detachment fault beneath the TAG hydrothermal mound at 26°N on the Mid-Atlantic Ridge [*deMartin et al.*, 2007]. However, our OBS array was not configured to locate seismicity east of the ridge axis and only covers a few months of activity, hence the asymmetry may be more apparent than real.

5. Focal Mechanisms for Earthquakes on the Atlantis Massif

[16] To determine the rupture mechanisms responsible for the events on the Massif, we measured the polarities of first-arrival P waves for 98 earthquakes relocated on the Massif using HYPODD and having a minimum of 8 arrival-time picks. A 1-D velocity model (Figure 7), derived from the 2-D velocity models presented in *Blackman and Collins* [2010], was used to calculate P wave take-off angles. Because event depths are not well constrained, and our 1-D velocity model is an approximation only to the true structure, the calculated take-off angles are also an approximation. Errors in take-off angles are

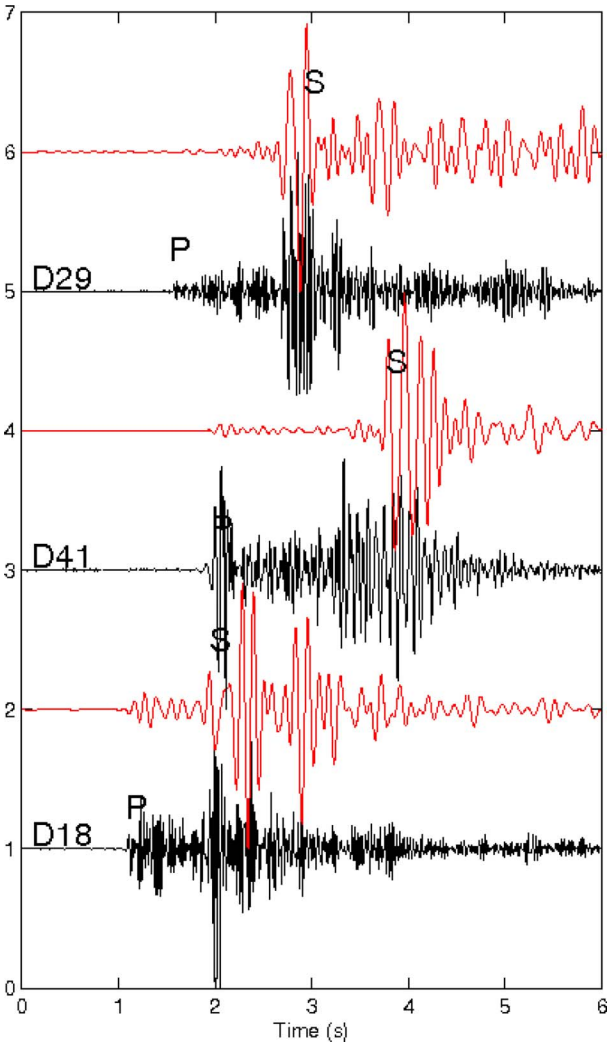

Figure 6. Vertical- (black) and horizontal-component (red immediately above) seismograms for the 3 stations closest to the Lost City hydrothermal vent field for an event located within the Massif. The P waves arrive first at station D18 (see Figure 2) and the ~1 s P – S time at station D18 demonstrates that this event is located within the Massif, as are many others (Figure 2).

explicitly accounted for in the determination of focal mechanisms, but for the purposes of plotting polarities we assumed a hypocentral depth of 4 km for all events.

[17] Earthquakes on the Massif cluster into two groups based on P wave first-motion polarities and time of occurrence (Figures 8–10). The predominant cluster on the Massif is active throughout the 6-month deployment, while a smaller, more localized cluster on the Massif is from a large swarm (~500+ earthquakes) that occurred on December 16 and 17, 2005 (red dots, Figure 11). We determined composite earthquake focal mechanisms for both clusters using the HASH algorithm [*Hardebeck and Shearer*, 2002, 2003; *Kilb and Hardebeck*, 2006]. This technique returns a set of acceptable focal mechanisms, taking into account user-specified errors in event location and velocity model, (or equivalently ray take-off angles and azimuths), and first-motion polarities. Solutions are deemed acceptable if the total number of misfit polarities is less than or equal to a user-specified maximum value. The average of the set of acceptable solutions is chosen as the preferred mechanism, and the solution uncertainty is measured by the root-mean square (RMS) angular difference between the acceptable mechanisms and the preferred mechanism. The quality of a mechanism is based on the tightness of the set of acceptable mechanisms and the number of misfit polarities associated with the preferred solution.

[18] For our study, we assumed Gaussian-distributed errors in take-off angle and azimuth with standard deviations of ±20° and ±5° respectively. The large assumed uncertainty in take-off angles reflects the poor constraints on earthquake depths, and for our velocity-depth model corresponds roughly with depth uncertainties of ±2 to 3 km.

[19] The HASH-derived preferred composite focal mechanism solutions for the two clusters are superimposed on their respective polarity distributions

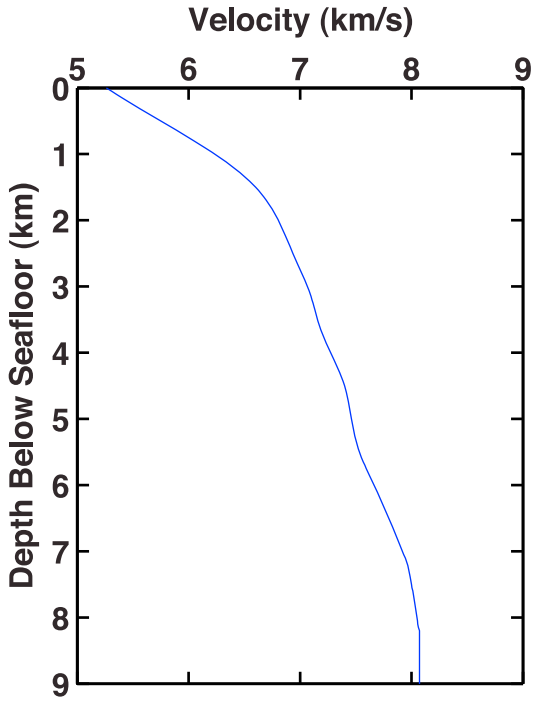

Figure 7. Velocity-depth curve used for estimating ray take-off angles. This curve is derived from the 2-D velocity models presented in *Blackman and Collins* [2010].

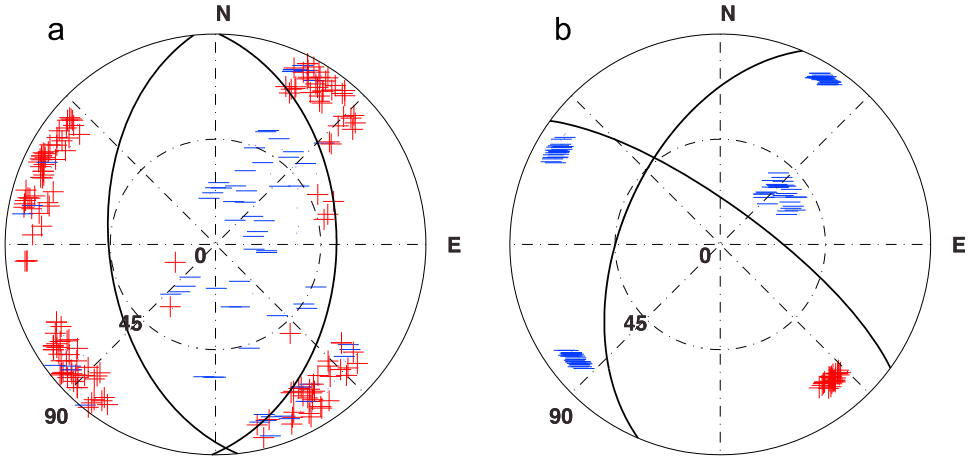

Figure 8. Polarities of first-motion P waves for events on the Atlantis Massif located using HYPODD and having a minimum of 8 arrival-time picks. Plots are lower hemisphere equal-area projections. The plotted coordinates are calculated assuming the 1-D velocity depth model shown in Figure 7 and event depths of 4 km below the seafloor. Red crosses and blue dashes represent compressional (ground motion up) and dilatational (ground motion down) particle displacements, respectively. (a) Polarities for the majority of events on the Massif, with epicenters shown with white symbols in Figure 11. The black curves show the focal mechanism preferred by the HASH algorithm, and is indicative of a north-south trending normal fault. The preferred strike, dip, and rake of the primary and auxiliary fault planes are 1°, 42°, and −85°, and 174°, 48°, and −94°, respectively. The average uncertainties in the strike, dip, and rake of the primary and auxiliary fault planes are both ±16°. (b) Polarities for a subset of events from an earthquake swarm that took place on December 16 and 17, 2005. These events, shown with red symbols in Figure 11, are spatially localized. The black curves show the focal mechanism preferred by the HASH algorithm, and is indicative of an approximately east-west trending strike-slip fault. The preferred strike, dip, and rake of the primary and auxiliary fault planes are 203°, 51°, and 160°, and 306°, 75°, and 41°, respectively. The average uncertainties in the strike, dip, and rake of the primary and auxiliary fault planes are ±27° and ±15°, respectively.

in Figures 9 and 10. The solutions for both clusters are of "A" quality, with an average RMS fault plane uncertainty of ≤25°, the fraction of misfit-polarities <=0.15, and a station distribution ratio ≥0.5.

[20] The preferred solution (Figures 8a and 9a) for events in the dominant cluster indicates normal faulting in an approximately ridge-parallel direction. Both nodal planes dip at ~45°, but since we do not know which nodal plane represents the fault surface, we cannot tell whether the fault dips toward or away from the axial rift valley. *deMartin et al.* [2007] present compelling evidence for ridge-parallel, antithetic normal faulting beneath the TAG

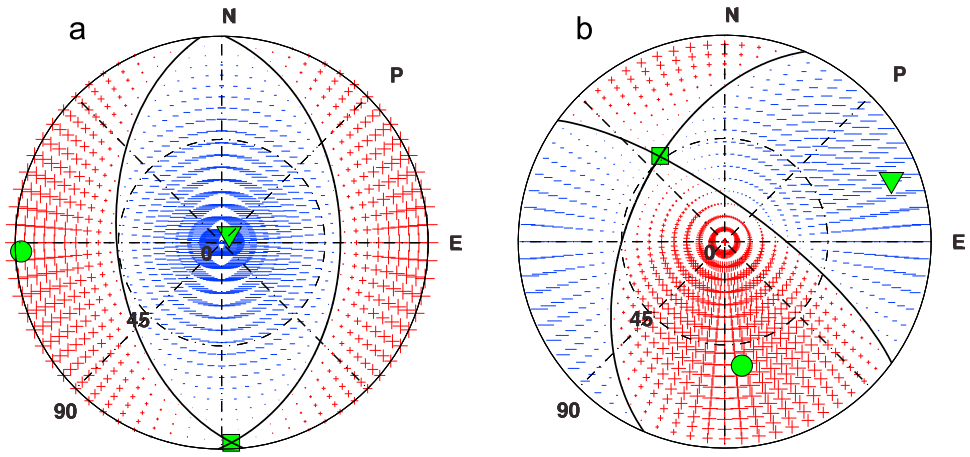

Figure 9. Predicted particle motion polarities and relative arrival amplitudes (lower hemisphere) for the preferred focal mechanism solutions given in Figure 8. The P- (inverted filled green triangle), T- (filled green circle), and B- (filled green square) axes are also shown.

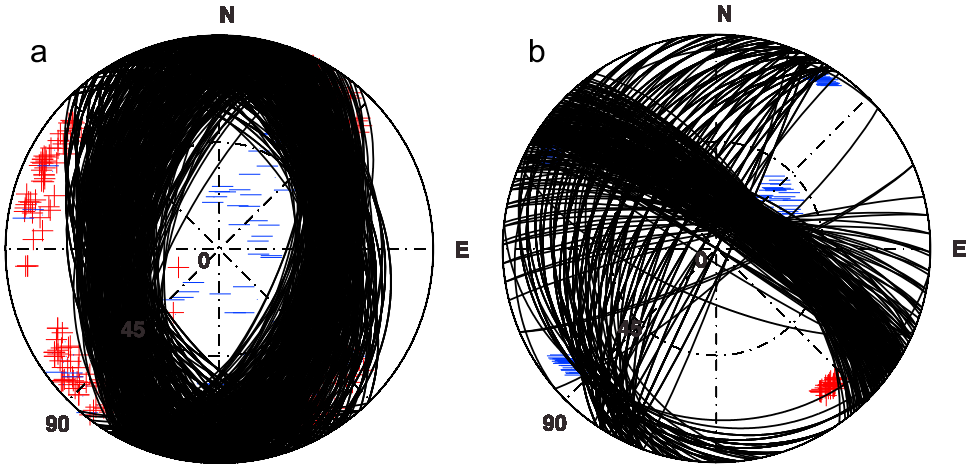

Figure 10. As for Figure 8, but with all acceptable focal mechanism solutions superimposed on the measured polarities. (a) All of the acceptable solutions are for normal faults. (b) The acceptable solutions are split approximately 50:50 between reverse (plunge of T-axis > 40°) and strike-slip faulting mechanisms. The strike and dip of the ~E-W, steeply dipping, nodal plane are much better constrained than for the conjugate plane. On geological grounds, we favor strike-slip motion on an approximately east-west plane.

detachment surface and near the rift valley wall. The set of acceptable solutions (Figure 10a) are all indicative of normal faulting with a trend approximately parallel to the ridge axis.

[21] The preferred composite focal mechanism solution for the second, smaller cluster indicates a strike-slip fault (Figures 8b and 9b). The approximately E-W nodal plane, which aligns well with the trend of the topographic scarp (~300°) and inferred geological boundary between South Ridge and Central Dome, would indicate a left-lateral strike-slip fault. The set of acceptable solutions (Figure 10b) ranges from strike-slip to reverse faulting.

6. Discussion and Conclusions

[22] The locations of the hydrophone-recorded seismicity and the OBS-recorded seismicity are shown in Figures 1 and 2. Although not acquired concurrently, and the OBS recorded earthquakes with magnitudes as small as 0–0.5 compared to the hydrophones with an estimated magnitude of completeness of about ~2.5 [*Bohnenstiehl et al.*, 2002], the two data sets have some similarities. They both indicate that there is seismic activity within the Atlantis Massif located primarily in the eastern section of South Ridge. Within the Massif, though, the OBS-located earthquakes tend to cluster near the north-facing scarp of South Ridge, while the hydrophone-located seismicity tends to be farther south where fewer earthquakes are located by the OBS array but where the bathymetry is shallower.

[23] Local magnitude estimates of the OBS-recorded earthquakes suggest that earthquakes within the Massif are small (ml < 2), and thus likely below the completeness level of the hydroacoustic-derived seismicity catalog [*Bohnenstiehl et al.*, 2002]. However, the detection of small magnitude events from this region with the hydroacoustic array is enhanced because the Massif summit protrudes into the SOFAR channel. The most dramatic difference between the two data sets is that ridge-axis earthquakes dominate the OBS data set, while they are limited in the hydrophone-recorded data set. In contrast to the earthquakes within the Massif, numerous ml > 2 OBS-recorded earthquakes are located within the axial valley. This suggests that the energy from earthquakes occurring within the deep sections of the ridge axis adjacent to the Atlantis Massif is not reaching the SOFAR channel and not being recorded by the hydrophones. In order to fully understand the differences in the spatial distribution of seismicity between the hydrophone and OBS earthquake catalogs and their relationship to earthquake magnitudes, however, will require a concurrent deployment of autonomous hydrophones and OBS.

[24] The active strike-slip and normal faulting within the Massif (Figures 8 and 9) is characteristic of inside corners, and is indicative of the low strength of transform faults. *Behn et al.* [2002] performed boundary element modeling of ridge-transform inside-corner regions, and concluded that shear-stress coupling across oceanic transform faults must be very small on geologic time scales to be

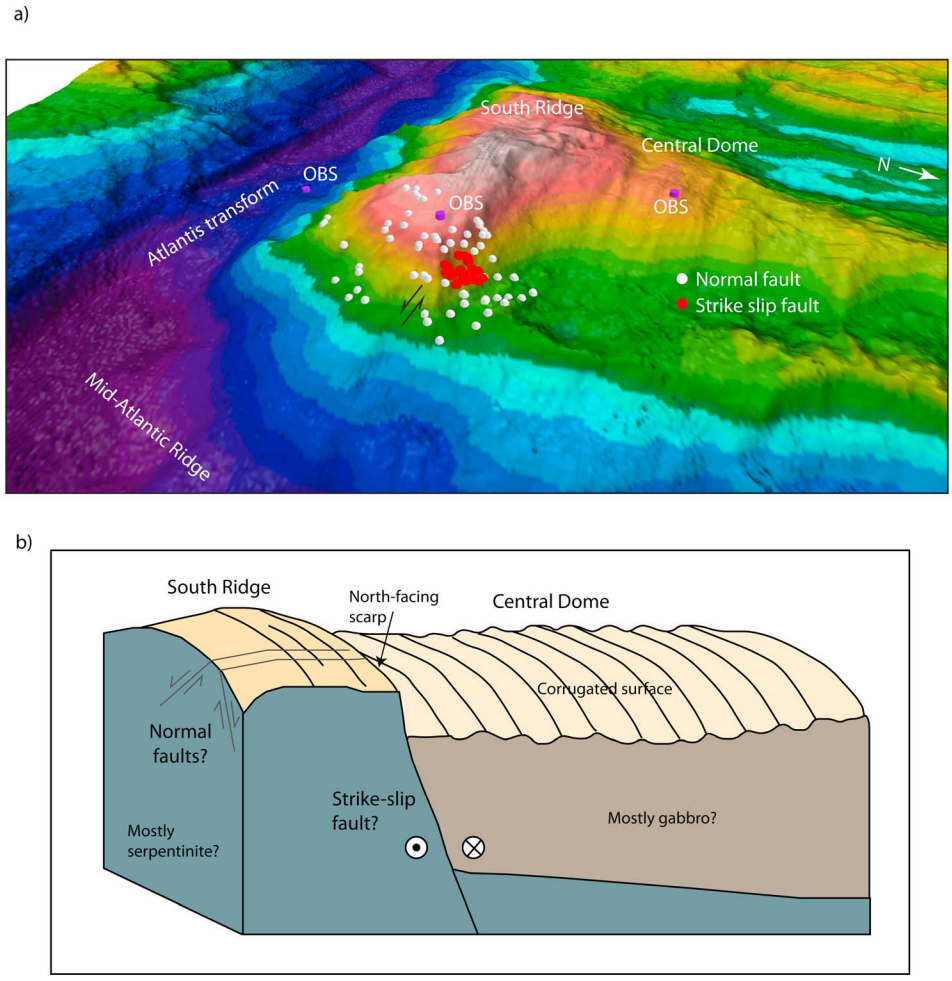

Figure 11. (a) A view of the Atlantis Massif from the northeast showing earthquakes that occurred within the Massif. The earthquakes cluster into two groups based on P wave first motion polarities and on time of occurrence. The predominant cluster (shown in white) is active throughout the deployment, while a smaller, more localized cluster (shown in red) is from a large swarm (~500+ earthquakes) that took place on December 16 and 17, 2005. P wave polarities for all of events shown here are plotted in Figure 9. (b) Schematic diagram of the Atlantis Massif viewed from the southeast showing a geologic interpretation of the Massif (adapted from *Karson et al.* [2006]). The OBS data indicate a left-lateral, strike-slip fault in the region of the north-facing scarp, which marks the boundary between South Ridge and Central Dome. The normal faults identified in the OBS data are shown schematically in cross-section on the south-facing scarp of South Ridge. It is not possible to determine whether the normal faults dip toward or away from the spreading axis.

consistent with observations of oblique normal faulting at inside corners. This oblique normal faulting has been observed primarily from seafloor morphology [e.g., *Gràcia et al.*, 1999] and focal mechanisms of moderate earthquakes calculated from teleseismic data [*Huang and Solomon*, 1988]. The curvature of the median valley seismicity toward the west as it approaches the Atlantis transform (Figure 2) is a direct demonstration that these oblique normal faults on the edge of the axial valley are active all the way to the ridge-transform intersection. The models by *Behn et al.* [2002] also predict that strike-slip faulting with the same sense of displacement as the main transform fault would occur at inside corners up to ~10 km from the main transform plate boundary, which is consistent with the location of the strike-slip events observed in our data.

[25] The extinct Atlantis Bank detachment formed in a similar setting as the Atlantis Massif. Atlantis Bank. It is located adjacent to the Atlantis II transform fault on the Southwest Indian Ridge [*Dick et al.*, 2000], and two transform-parallel normal faults have formed approximately 25 km east of the

transform. The faults face away from the transform and extend about 15 km along strike. *Baines et al.* [2003] suggested that these faults formed during or very close to the time of detachment faulting and are consistent with the *Behn et al.* [2002] model. *Baines et al.* [2003] also suggested though, that the large normal slip (hundreds of meters) observed on the two transform-parallel faults may have been produced after the cessation of detachment faulting, when local stresses reoriented during transtension at the adjacent transform. In contrast, at the Atlantis Massif the transform parallel fault has very high relief (~1500 m) immediately adjacent to the axial valley, and must have formed during detachment faulting.

[26] Because the slip on the north-facing scarp between South Ridge and Central Dome decreases to the west from ~1500 m adjacent to the axial valley to ~400 m where South Ridge and Central Dome meet, the strike-slip events might also indicate an oblique tear or scissor fault. A tear fault could result from differential movement on adjacent fault surfaces. In this case, there would be a dip-slip component, which we cannot determine with the data in hand (Figure 8b). In addition, the active ridge-parallel normal faulting on the Massif might be associated with deformation of the detachment surface. Assuming that a normal fault initiates at the axis with a dip of ~60° [*Buck*, 1988], as much as 20° of fault rotation can occur within 5 km of the spreading axis [*Schouten et al.*, 2010]. If extension on a single fault continues for more than about 5 km, the exhumed fault surface flattens and domes as a result of regional isostatic compensation [*Buck*, 1988]. The seismicity in the eastern section of South Ridge and the volcanic block is ~6–10 km from the spreading axis and thus, may be related to the flexural bending of the detachment surface.

[27] Is the Atlantis Massif detachment fault still active? Several studies have suggested that asymmetric spreading is a characteristic feature of detachment faulting [*Baines et al.*, 2008; *Okino et al.*, 2004; *Searle et al.*, 2003], and *Grimes et al.* [2008] concluded that asymmetric spreading occurred for at least 200 ka during the development of the Atlantis Massif. There is some suggestion that the seismicity recorded by the OBS array is primarily located on the western bounding fault of the axial valley indicating asymmetric spreading and perhaps active detachment faulting, although the pilot array that we deployed was not configured to address this question.

[28] Our plan had been to deploy the OBS array before the hydrophone array was retrieved in order to compare earthquake catalogs. For various reasons this was not achieved. We think though, that our pilot project with a modest number of OBSs provides new information on present-day seismicity and deformation within the Atlantis Massif and the adjacent spreading axis. Unfortunately, the OBS data cannot address all of the outstanding questions, but they provide the foundation for a more comprehensive experiment to enhance our understanding of how spreading occurs at a segment of the slow-spreading MAR that has been dominated by detachment faulting for long periods of its history.

Acknowledgments

[29] We thank the Deep Ocean Exploration Institute at WHOI, Director of Research at WHOI, WHOI's Department of Geology and Geophysics, and the National Science Foundation for funding the data collection. DKS had fruitful discussions with D. Blackman, J. Karson, B. John, J. Cann, J. Escartin, and H. Schouten. We thank Del Bohnenstiehl and an anonymous reviewer for their very constructive suggestions and comments. The OBS were deployed by Peter Lemmond (WHOI), Matt Fowler (OSU), and Cedric Brachett (Université de Brest) on cruise KN182–3 of the R/V Knorr, and recovered by David Dubois (WHOI) on cruise EN-415 of the R/V Endeavor. We thank the officers and crews of both vessels for their efforts in making this experiment a success. JAC thanks Götz Bokelmann (University of Vienna) for his hospitality during the writing of this paper.

References

Baines, A. G., M. J. Cheadle, H. J. B. Dick, A. Hosford, B. E. John, and J. J. Schwartz (2003), Mechanism for generating the anomalous uplift of oceanic core complexes: Atlantis Bank, southwest Indian Ridge, *Geology*, *31*, 1105–1108, doi:10.1130/G19829.19821.

Baines, A. G., M. J. Cheadle, B. E. John, and J. J. Schwartz (2008), The rate of oceanic detachment faulting at Atlantis Bank, SW Indian Ridge, *Earth Planet. Sci. Lett.*, *273*(1–2), 105–114, doi:10.1016/j.epsl.2008.06.013.

Behn, M. D., J. Lin, and M. T. Zuber (2002), Mechanisms of normal fault development at mid-ocean ridges, *J. Geophys. Res.*, *107*(B4), 2083, doi:10.1029/2001JB000503.

Blackman, D. K., and J. A. Collins (2010), Lower crustal variability and the crust/mantle transition at the Atlantis Massif oceanic core complex, *Geophys. Res. Lett.*, *37*, L24303, doi:10.1029/2010GL045165.

Blackman, D. K., J. R. Cann, B. Janssen, and D. K. Smith (1998), Origin of extensional core complexes: Evidence from the Mid-Atlantic Ridge at Atlantis Fracture Zone, *J. Geophys. Res.*, *103*, 21,315–21,333, doi:10.1029/98JB01756.

Blackman, D. K., et al. (2002), Geology of the Atlantis Massif (Mid-Atlantic Ridge, 30°N): Implications for the evolution

of an ultramafic oceanic core complex, *Mar. Geophys. Res.*, *23*, 443–469, doi:10.1023/B:MARI.0000018232.14085.75.

Blackman, D. K., et al. (2011), Drilling constraints on lithospheric accretion and evolution at Atlantis Massif, Mid-Atlantic Ridge 30°N, *J. Geophys. Res.*, *116*, B07103, doi:10.1029/2010JB007931.

Bohnenstiehl, D. R., M. Tolstoy, R. P. Dziak, C. G. Fox, and D. K. Smith (2002), Aftershock sequences in the mid-ocean ridge environment: An analysis using hydroacoustic data, *Tectonophysics*, *354*, 49–70, doi:10.1016/S0040-1951(02)00289-5.

Buck, W. R. (1988), Flexural rotation of normal faults, *Tectonics*, *7*(5), 959–973, doi:10.1029/TC007i005p00959.

Canales, J. P., B. E. Tucholke, and J. A. Collins (2004), Seismic reflection imaging of an oceanic detachment megamullion (Mid-Atlantic Ridge, 30°10′N), *Earth Planet. Sci. Lett.*, *222*, 543–560, doi:10.1016/j.epsl.2004.02.023.

Canales, J. P., R. A. Sohn, and B. J. deMartin (2007), Crustal structure of the TAG segment (Mid-Atlantic Ridge, 26°10′N): Implications for the nature of hydrothermal circulation and detachment faulting at slow spreading ridges, *Geochem. Geophys. Geosyst.*, *8*, Q08004, doi:10.1029/2007GC001629.

Canales, J. P., B. E. Tucholke, M. Xu, J. A. Collins, and D. L. Dubois (2008), Seismic evidence for large-scale compositional heterogeneity of oceanic core complexes, *Geochem. Geophys. Geosyst.*, *9*, Q08002 doi:10.1029/2008GC002009.

Cann, J. R., D. K. Blackman, D. K. Smith, E. McAllister, B. Janssen, S. Mello, E. Avgerinos, A. R. Pascoe, and J. Escartín (1997), Corrugated slip surfaces formed at North Atlantic ridge-transform intersections, *Nature*, *385*, 329–332, doi:10.1038/385329a0.

Cannat, M., D. Sauter, V. Mendel, E. Ruellan, K. Okino, J. Escartin, V. Combier, and M. Baala (2006), Modes of seafloor generation at a melt-poor ultraslow-spreading ridge, *Geology*, *34*(7), 605–608, doi:10.1130/G22486.1.

Collins, J. A., D. K. Blackman, A. Harris, and R. L. Carlson (2009), Seismic and drilling constraints on velocity structure and reflectivity near IODP Hole U1309D on the central dome of Atlantis Massif, Mid-Atlantic Ridge 30°N, *Geochem. Geophys. Geosyst.*, *10*, Q01010, doi:10.1029/2008GC002121.

deMartin, B. J., R. A. Reves-Sohn, J. P. Canales, and S. E. Humphris (2007), Kinematics and geometry of active detachment faulting beneath the TAG hydrothermal field on the Mid-Atlantic Ridge, *Geology*, *35*(8), 711–714, doi:10.1130/G23718A.1.

Dick, H. J. B., G. Thompson, and W. B. Bryan (1981), Low angle faulting and steady-state emplacement of plutonic rocks at ridge-transform intersections, *Eos Trans. AGU*, *62*, 406.

Dick, H. J. B., et al. (2000), A long *In Situ* section of the lower ocean crust: Results of ODP leg 176 drilling at the Southwest Indian Ridge, *Earth Planet. Sci. Lett.*, *179*, 31–51, doi:10.1016/S0012-821X(00)00102-3.

Dziak, R. P., D. R. Bohnenstiehl, H. Matsumoto, C. G. Fox, D. K. Smith, M. Tolstoy, T.-K. Lau, J. H. Haxel, and M. J. Fowler (2004), P- and T-wave detection thresholds, Pn velocity estimate, and detection of lower mantle and core P-waves on ocean sound-channel hydrophones at the Mid-Atlantic Ridge, *Bull. Seismol. Soc. Am.*, *94*, 665–677, doi:10.1785/0120030156.

Escartín, J., and M. Cannat (1999), Ultramafic exposures and the gravity signature of the lithosphere near the Fifteen-Twenty Fracture Zone (Mid-Atlantic Ridge, 14°–16.5°N), *Earth Planet. Sci. Lett.*, *171*, 411–424, doi:10.1016/S0012-821X(99)00169-7.

Escartín, J., D. K. Smith, J. Cann, H. Schouten, C. H. Langmuir, and S. Escrig (2008), Central role of detachment faults in accretion of slow-spread oceanic lithosphere, *Nature*, *455*, 790–794, doi:10.1038/nature07333.

Expedition Scientific Party (2005), *Oceanic Core Complex Formation, Atlantis Massif*, *Integrated Ocean Drill. Program Prelim. Rep.*, *304*. [Available at http://iodp.tamu.edu/publications/PR/304PR/304PR.PDF]

Gràcia, E., D. Bideau, R. Hekinian, and Y. Lagabrielle (1999), Detailed geological mapping of two contrasting second-order segments of the Mid-Atlantic Ridge between Oceanographer and Hayes fracture zones (33°30′N–35°N), *J. Geophys. Res.*, *104*, 22,903–22,921.

Grimes, C. B., B. E. John, M. J. Cheadle, and J. L. Wooden (2008), Protracted construction of gabbroic crust at a slow spreading ridge: Constraints from $^{206}Pb/^{238}U$ zircon ages from Atlantis Massif and IODP Hole U1309D (30°N, MAR), *Geochem. Geophys. Geosyst.*, *9*, Q08012, doi:10.1029/2008GC002063.

Hardebeck, J. L., and P. M. Shearer (2002), A new method for determining first-motion focal mechanisms, *Bull. Seismol. Soc. Am.*, *92*, 2264–2276, doi:10.1785/0120010200.

Hardebeck, J. L., and P. M. Shearer (2003), Using S/P amplitude ratios to constrain the focal mechanisms of small earthquakes, *Bull. Seismol. Soc. Am.*, *93*(6), 2434–2444, doi:10.1785/0120020236.

Henig, A. S., D. K. Blackman, A. J. Harding, J. P. Canales, and G. M. Kent (2012), Downward continued multichannel seismic refraction analysis of Atlantis Massif oceanic core complex, 30°N, Mid-Atlantic Ridge, *Geochem. Geophys. Geosyst.*, *13*, Q0AG07, doi:10.1029/2012GC004059.

Huang, P., and S. C. Solomon (1988), Centroid depths of mid-ocean ridge earthquakes: Dependence on spreading rate, *J. Geophys. Res.*, *93*, 13,445–13,477, doi:10.1029/JB093iB11p13445.

Ildefonse, B., D. K. Blackman, B. E. John, Y. Ohara, D. J. Miller, C. J. MacLeod, and Integrated Ocean Drilling Program Expeditions 304/305 Science Party (2007), Oceanic core complexes and crustal accretion at slow-spreading ridges, *Geology*, *35*, 623–626, doi:10.1130/G23531A.23531.

Karson, J. A. (1999), Geological investigation of a lineated massif at the Kane Transform Fault: Implications for oceanic core complexes, *Philos. Trans. R. Soc.*, *357*, 713–740, doi:10.1098/rsta.1999.0350.

Karson, J. A., G. L. Früh-Green, D. S. Kelley, E. A. Williams, D. R. Yoerger, and M. Jakuba (2006), Detachment shear zone of the Atlantis Massif Core Complex, Mid-Atlantic Ridge 30°N, *Geochem. Geophys. Geosyst.*, *7*, Q06016, doi:10.1029/2005GC001109.

Kelemen, P. B., et al. (2004), *Initial Reports of the Ocean Drilling Program*, vol. 209, Ocean Drill. Program, College Station, Tex., doi:10.2973/odp.proc.ir.209.2004.

Kelley, D. S., et al. (2001), The Lost City Hydrothermal Field: A peridotite-hosted, off-axis system at 30°N on the Mid-Atlantic Ridge, *Nature*, *412*, 145–149, doi:10.1038/35084000.

Kelley, D. S., J. A. Karson, G. L. Früh-Green, D. R. Yoerger, T. M. Shank, D. A. Butterfield, J. M. Hayes, M. O. Schrenk, E. Olson, and G. Proskurowski (2005), A serpentinite-hosted ecosystem: The Lost City Hydrothermal Field, *Science*, *307*, 1428–1434, doi:10.1126/science.1102556.

Kilb, D., and J. L. Hardebeck (2006), Fault parameter constraints using relocated earthquakes: A validation of first-motion focal-mechanism data, *Bull. Seismol. Soc. Am.*, *96*(3), 1140–1158, doi:10.1785/0120040239.

MacLeod, C. J., et al. (2002), Direct geological evidence for oceanic detachment faulting: The Mid-Atlantic Ridge,

15°45′N, *Geology*, *30*(10), 879–882, doi:10.1130/0091-7613(2002)030<0879:DGEFOD>2.0.CO;2.

McGuire, J. J. (2008), Seismic cycles and earthquake predictability on East Pacific Rise transform faults, *Bull. Seismol. Soc. Am.*, *98*, 1067–1084, doi:10.1785/0120070154.

Okino, K., K. Matsuda, D. Christie, Y. Nogi, and K. Koizumi (2004), Development of oceanic detachment and asymmetric spreading at the Australian-Antarctic Discordance, *Geochem. Geophys. Geosyst.*, *5*, Q12012, doi:10.1029/2004GC000793.

Pan, J., and A. M. Dziewonski (2005), Comparison of mid-oceanic earthquake epicentral differences of travel time, centroid locations, and those determined by autonomous underwater hydrophone arrays, *J. Geophys. Res.*, *110*, B07302, doi:10.1029/2003JB002785.

Reston, T. J., and C. R. Ranero (2011), The 3-D geometry of detachment faulting at mid-ocean ridges, *Geochem. Geophys. Geosyst.*, *12*, Q0AG05, doi:10.1029/2011GC003666.

Schaff, D. P., G. H. R. Bokelmann, G. C. Beroza, F. Waldhauser, and W. L. Ellsworth (2002), High-resolution image of Calaveras Fault seismicity, *J. Geophys. Res.*, *107*(B9), 2186, doi:10.1029/2001JB000633.

Schaff, D. P., G. H. R. Bokelmann, W. L. Ellsworth, E. Zanzerkia, F. Waldhauser, and G. C. Beroza (2004), Optimizing correlation techniques for improved earthquake location, *Seism. Soc. Am.*, *94*, 705–721, doi:10.1785/0120020238.

Schouten, H., D. K. Smith, J. R. Cann, and J. Escartin (2010), Tectonic versus magmatic extension in the presence of core complexes at slow-spreading ridges from a visualization of faulted seafloor topography, *Geology*, *38*, 615–618, doi:10.1130/G30803.30801.

Schroeder, T. J., and B. E. John (2004), Strain localization on an oceanic detachment fault system, Atlantis Massif, 30°N, Mid-Atlantic Ridge, *Geochem. Geophys. Geosyst.*, *5*, Q11007, doi:10.1029/2004GC000728.

Searle, R. C., M. Cannat, K. Fujioka, C. Mevel, H. Fujimoto, A. Bralee, and L. Parson (2003), FUJI Dome: A large detachment fault near 64°E on the very slow-spreading southwest Indian Ridge, *Geochem. Geophys. Geosyst.*, *4*(8), 9105, doi:10.1029/2003GC000519.

Simão, N., J. Escartín, J. Goslin, J. Haxel, M. Cannat, and R. Dziak (2010), Regional seismicity of the Mid-Atlantic Ridge: Observations from autonomous hydrophone arrays, *Geophys. J. Int.*, *183*(3), 1559–1578, doi:10.1111/j.1365-246X.2010.04815.x.

Simons, F. J., B. D. E. Dando, and R. M. Allen (2006), Automatic detection and rapid determination of earthquake magnitude by wavelet multiscale analysis of the primary arrival, *Earth Planet. Sci. Lett.*, *250*, 214–223, doi:10.1016/j.epsl.2006.1007.1039.

Smith, D. K., M. Tolstoy, C. G. Fox, D. R. Bohnenstiehl, H. Matsumotu, and M. J. Fowler (2002), Hydroacoustic monitoring of seismicity at the slow-spreading Mid-Atlantic Ridge, *Geophys. Res. Lett.*, *29*(11), 1518, doi:10.1029/2001GL013912.

Smith, D. K., J. Escartin, M. Cannat, M. Tolstoy, C. G. Fox, D. Bohnenstiehl, and S. Bazin (2003), Spatial and temporal distribution of seismicity along the northern Mid-Atlantic Ridge (15°–35°N), *J. Geophys. Res.*, *108*(B3), 2167, doi:10.1029/2002JB001964.

Smith, D. K., J. R. Cann, and J. Escartin (2006), Widespread active detachment faulting and core complex formation near 13°N on the Mid-Atlantic Ridge, *Nature*, *442*, 440–443, doi:10.1038/nature04950.

Smith, D. K., J. Escartin, H. Schouten, and J. R. Cann (2008), Fault rotation and core complex formation: Significant processes in seafloor formation at slow-spreading mid-ocean ridges (Mid-Atlantic Ridge, 13–25°N), *Geochem. Geophys. Geosyst.*, *9*, Q03003, doi:10.1029/2007GC001699.

Tucholke, B. E., J. Lin, and M. C. Kleinrock (1998), Megamullions and mullion structure defining oceanic metamorphic core complexes on the mid-Atlantic ridge, *J. Geophys. Res.*, *103*, 9857–9866, doi:10.1029/98JB00167.

Waldhauser, F. (2001), hypoDD—A program to compute double-difference hypocenter locations, *U.S. Geol. Surv. Open File Rep.*, *01-113*, 25 pp.

Waldhauser, F., and W. L. Ellsworth (2000), A double-difference earthquake location algorithm: Method and application to the northern Hayward fault, California, *Bull. Seismol. Soc. Am.*, *90*, 1353–1368, doi:10.1785/0120000006.

Williams, C. M., R. A. Stephen, and D. K. Smith (2006), Hydroacoustically recorded seismicity at the intersection of the Atlantis (30°N) and Kane (23°40′N) Transform Faults with the Mid-Atlantic Ridge, *Geochem. Geophys. Geosyst.*, *7*, Q06015, doi:10.1029/2005GC001127.